Plasmonics
https://doi.org/10.1007/s11468-020-01313-5

Design of Sub wavelength-Grating-Coupled Fano Resonance Sensor in Mid-infrared

Yuhan Wang[1] · Dianhong Wang[1] · Xiangli Zhang[1] · Tianye Huang[1] · Xiang Zhao[1] · Shuwen Zeng[2]

Received: 5 August 2020 / Accepted: 15 October 2020
© Springer Science+Business Media, LLC, part of Springer Nature 2020

Abstract
By introducing the sub-wavelength grating (SWG) waveguide in the long-range surface phonon resonance (LRSPhR) device, a mid-infrared Fano resonance is formed due to the coupling between surface phonon polariton and Bloch mode. By taking advantage of strong light-matter interaction in the SWG, such Fano resonance is expected to offer improved sensing performance. Based on the rigorous coupled-wave analysis (RCWA) method, the index sensitivity and figure of merit of such a sensor reach 7496 RIU^{-1} and 46,432, respectively, which is 6 times compared with the conventional waveguide-coupled LRSPhR. The proposed SWG-coupled Fano resonance can be a promising platform for mid-infrared biochemical sensing.

Keywords Fano resonance · Mid-infrared · Long-range surface phonon resonance · Sub-wavelength grating

Introduction

Surface plasmon resonance (SPR) is a guided mode propagating along flat planar and sensitive to the changes in the environment. Under the phase-matching condition, the coupling between the incident light with the surface-guided mode can be achieved through the attenuated total reflection (ATR) mechanism [1–3]. Surface plasmon resonance (SPR)-based sensors have gained wide interests in medicine, environmental monitoring, and security [4, 5]. Over the past years, researches on SPR sensors based on noble metals such as Au and Ag have mainly limited in the visible and near-infrared (NIR) wavelength regime [6, 7]. In longer wavelength, e.g., mid-infrared (MIR), the conventional metals behave as perfect conductors with strong intrinsic loss, which limits the excitation of the SPR effect [8, 9]. To implement sensors in MIR, people have explored the use of polar dielectric materials, which supports the surface phonon polaritons (SPhPs). The lifetime of SPhP mode could be up to picosecond order, which is one to two orders longer than that of surface plasmon polariton (SPP) mode [10–12]. With the coupling between optical photons and SPhPs, surface phonon resonance (SPhR) can be excited. Based on such characteristics, SPhR has been considered as a low loss alternative of SPR in MIR.

The SPhR effect offers a promising approach to implement the refractive index (RI) sensor in the MIR. From the viewpoint of precise sensing, the most important two parameters are the sensing accuracy and figure of merit (FOM). In order to increase the sensing accuracy, the resonance should be as narrow as possible to precisely estimate the resonance angle change. For this purpose, Fano resonance (FR) with asymmetric line shape is regarded as an effective method [13–18]. FR originates from the coupling between SPP/SPhP mode and waveguide photonic mode. In order to further enhance the sensing performance, it is desired to enlarge the contacting area between the waveguide surface and sensing medium. Recently, sub-wavelength grating (SWG) whose period is much smaller than the operation wavelength has been widely investigated. This is because the SWG can support Bloch mode with tailorable dispersion properties and low loss [19–24]. From the viewpoint of sensing, the smaller duty ratio compared with the conventional waveguide can further increase the light-matter interaction [25, 26]. It is expected that, by introducing SWG in the FR-based index sensor, the performance can be enhanced.

✉ Xiangli Zhang
zhangxiangli@cug.edu.cn

✉ Tianye Huang
tianye_huang@163.com

[1] School of Mechanical Engineering and Electronic Information, China University of Geosciences (Wuhan), Wuhan 430074, Hubei, China

[2] XLIM Research Institute, University of Limoges, 87032 Limoges, France

Published online: 24 October 2020

In this paper, a new SWG-coupled long-range surface phonon resonance (SWG-LRSPhR) sensor operating in the MIR wavelength region is proposed. The coupling between SPhP mode and SWG Bloch mode forms the FR line shape. The overlap between the electromagnetic field and the sensing medium is enhanced due to the enlarged contacting surface of the SWG waveguide. Furthermore, to better assess the sensing performance, both the sensitivity and FOM are investigated in detail. Such configuration can be used in various bio- and chemical-sensing applications.

Materials and Methods

The structure for conventional stripe waveguide-coupled long-range surface phonon resonance (WG-LRSPhR) based on Kretschmann configuration is shown in Fig. 1a. With the homogeneous ZnSe layer replaced by the ZnSe grating, the SWG-LRSPhR sensor can be formed, as shown in Fig. 1b.

Both structures consist of a germanium (Ge) prism, barium fluoride (BaF_2), silicon carbide (SiC), barium fluoride, zinc selenide (ZnSe), and the sensing medium layer. For the initial investigation, the following parameters are used: the thickness of BaF_2 layer $d_1 = 4$ μm, SiC layer $t = 0.7$ μm, BaF_2 layer $d_2 = 8$ μm, ZnSe layer $h_g = 2.8$ μm, the grating period $\Lambda = 0.5$ μm, and the grating width $w_g = 0.25$ μm. In the absence of free charge carriers, the frequency-dependent complex dielectric permittivity of SiC can be given as [27–29]:

$$\varepsilon_{SiC} = \varepsilon'_{SiC} + i\varepsilon''_{SiC} = \varepsilon_\infty \frac{\omega^2 - \omega_{LO}^2 + i\gamma\omega}{\omega^2 - \omega_{TO}^2 + i\gamma\omega} \quad (1)$$

where the optical phonon frequency $\omega_{LO} = 972$ cm^{-1}, the transverse optical phonon frequency $\omega_{TO} = 796$ cm^{-1}, the damping rate $\gamma = 3.75$ cm^{-1}, and the high-frequency dielectric constant $\varepsilon_\infty = 6.5$. With wavelength ranges from 10 to 15 μm, the Reststrahlen band defined by $\varepsilon'_{SiC} < 0$ corresponds to $\omega_{TO} < \omega < \omega_{LO}$ that is shown in Fig. 2. With the negative dielectric constant real part, SPhP modes can be supported. At $\lambda = 10.8$ μm, the period of ZnSe grating $\Lambda = 0.5$ μm, about one-twentieth of the wavelength, matching the propagating light condition and SWG behaves as the homogeneous metamaterial [20, 23]. The corresponding refractive indexes used are $n_p = 4.0037$ for the Ge prism, $n_{BaF2} = 1.3919$ for BaF_2, $n_{ZnSe} = 2.3950$ for ZnSe, and $n_s = 1.332$ for the sensing medium [30].

With the structure parameters mentioned above, the ATR curve of TM-polarized light calculated by rigorous coupled-wave analysis (RCWA) method [31–34] is shown in Fig. 3a. On the left side of LRSPhR, a sharp asymmetric FR arises. There are three dips with the incident angle ranging from 20 to 25°, denoted as 'A', 'B', and 'C', respectively, where

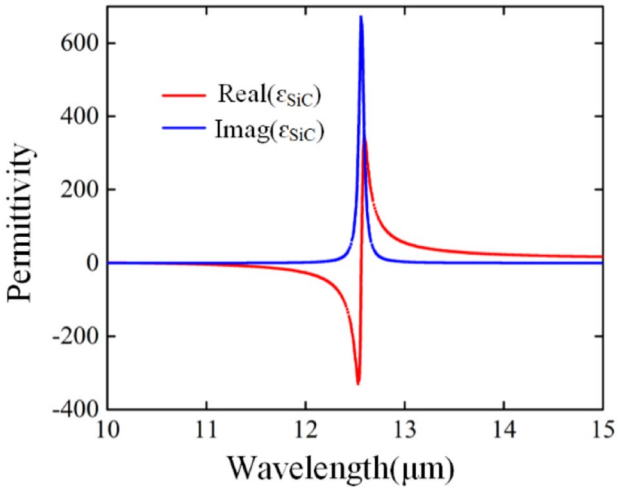

Fig. 2 The real part (red line) and imaginary part (blue line) of the permittivity of SiC, following the Drude-Lorentz model

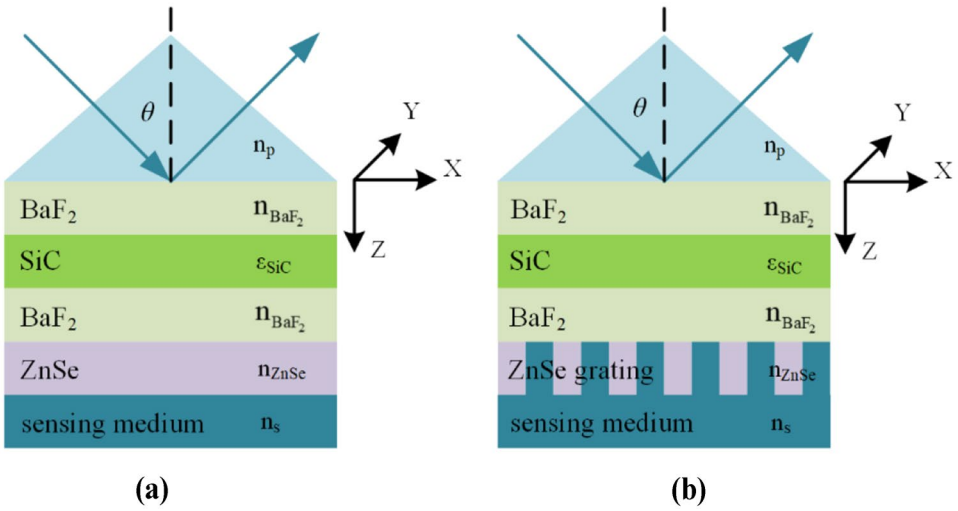

Fig. 1 **a** Structure of the WG-LRSPhR sensor consisting of the Ge prism, BaF_2, SiC, BaF_2, ZnSe, and sensing medium. **b** Structure of the SWG sensor consisting of the Ge prism, BaF_2, SiC, BaF_2, ZnSe grating, and sensing medium

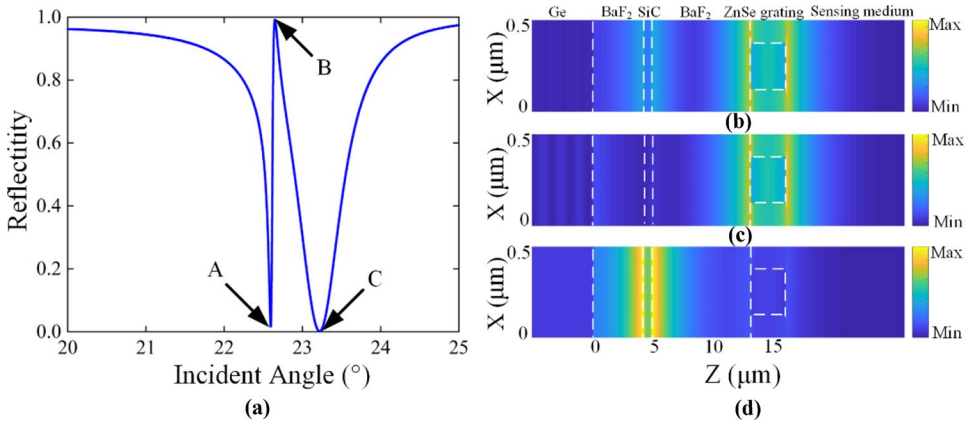

Fig. 3 **a** ATR curve of the sub-wavelength grating structure. **b–d** Electric field distributions at A, B, C in Fig. 3a with RI of sensing medium of 1.332

the value of *Z*-axis represents the distance from each layer to the prism surface. Fig. 3 b and c show the electric field distributions of the dip 'A', 'B' at 22.5944 and 22.6483°, respectively. It is revealed that large electric fields appear around ZnSe grating, caused by the coupling between Bloch mode and SPhP. Fig. 3 d corresponds to the dip 'C' at 23.2190°. Strong symmetric electric fields generated at the BaF_2-SiC-BaF_2 interface and decay exponentially away from the interface, indicating the excitation of LRSPhP mode.

Fano resonance exhibits a sharp asymmetric profile due to the strongly trapped resonance, where the reflectance can drop sharply from the peak to the valley of the spectra. High sensitivity can be provided to the index variations of the nearby or surrounding medium because of such a small angle change. Fig. 4 a shows that with the parameters fixed and the RI of sensing medium ranging from 1.332 to 1.333, the FR shifts to a larger angle.

The detectable change of RI determines the quality of the sensor. For evaluating the performance of the sensor, sensitivity (S) and FOM are given as follows:

$$S(\theta) = \lim_{\Delta n \to 0} \frac{\Delta R(\theta)}{\Delta n} = \frac{\partial R(\theta)}{\partial n} \tag{2}$$

$$\mathrm{FOM} = \Delta R/(R^{*}\Delta n) \tag{3}$$

where ΔR is the change of reflectivity caused by the change of index Δn, R denotes the reflectance in the proposed structure [30, 35]. With Δn = 10–3, Fig. 4b shows the sensitivity as a function of the incident angle. The peak of the curve in Fig. 4b is defined as Smax, which is employed to compare the sensitivities to different types of sensors.

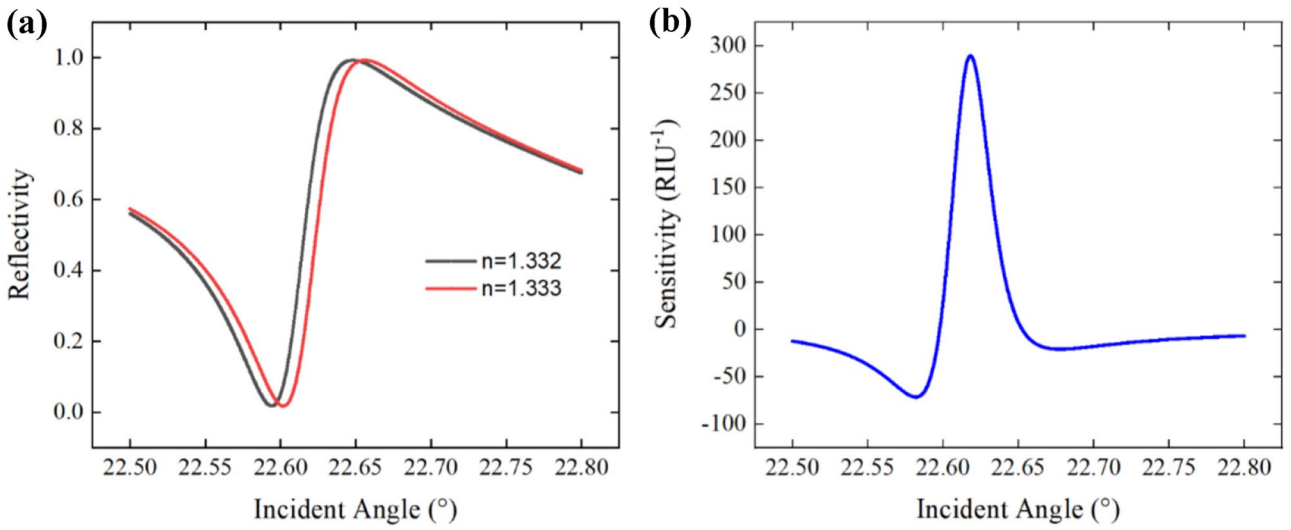

Fig. 4 **a** Variation in ATR curves with respect to the RI of sensing medium ranging from 1.332 to 1.333. **b** Sensitivity as a function of incident angle with $\Delta n = 0.001$

Results and Discussions

For further optimization, we investigate the sensing performance as function of period, duty ratio, height of grating layer, and thickness of BaF_2, respectively. Fig. 5 a demonstrates the variation of ATR curves with the thickness of the BaF_2 layer varying from 8.0 to 12.0 μm. Apparently, with a thicker BaF_2 layer, the coupling between Bloch mode and SPhP is weaker, resulting in a narrower FR. Also, it is obvious that narrower resonance makes a sharper FR curve, leading to higher sensitivity and FOM. Variations of the sensitivity and FOM as functions of BaF_2 thickness are shown in Fig. 5 b and c, respectively. The sensitivity and FOM keep increasing with the increment of the thickness of BaF_2. With $d_2 = 12.0$ μm, they are 5675 RIU^{-1} and 70,586, respectively.

ATR curves under different grating height are calculated and plotted in Fig. 5d, with d_2 fixed at 12 μm. It is clearly shown that with the increment of grating height, the resonant angle of FR keeps increasing, but the resonant shape remains almost unchanged. Fig. 5 e and f show the variations of sensitivity and FOM with ZnSe grating height ranging from 2.55 to 3.5 μm. Both sensitivity and FOM experience sharp fall before maximizing at $d_3 = 3.4$ μm and 3.25 μm, respectively. This can be attributed that when the resonant peaks of Bloch mode and SPhP get too close, the two modes interact with each other drastically. The FR becomes more like symmetric electromagnetic induced transparency (EIT) shape with a broader resonant angle.

Fig. 6 a shows the variation of ATR curves with various periods of ZnSe grating. When the period is in the range from 0.5 to 2.5 μm, the LRSPhR angle remains almost unchanged. However, according to Fig. 6 b and c, with the increment of the period, both sensitivity and FOM increase exponentially. This is because a larger period offers a larger contacting area for the sensing medium.

Fig. 6 d shows the variation of ATR curves with duty ratio ranging from 40 to 60%. The resonant angles of FR keep increasing from the left side to the right side of SPhR. Fig. 6 f illustrates the FOM of the proposed SWG sensor maximized with a duty ratio of 57.5%.

Moreover, in order to compare the performances between the SWG-LRSPhR sensor and conventional WG-LRSPhR sensor, sensitivity and FOM have been calculated with BaF_2 thickness ranging from 8.0 to 12.0 μm, as shown in Fig. 7a–d. Noted that with the height of the ZnSe layer of WG-LRSPhR sensor fixed at 1.7 μm, 1.8 μm, 1.9 μm, and 2.0 μm, we adjust the grating height of SWG-LRSPhR sensor to ensure the same resonant angle for comparison. Also, in order to track the sharp slope within the dynamic regime, the change of RI Δn and angle resolution $\Delta\theta$ have been resized. As shown in Fig. 7a–d, the SWG-LRSPhR sensor has good monotonicity and better performance than

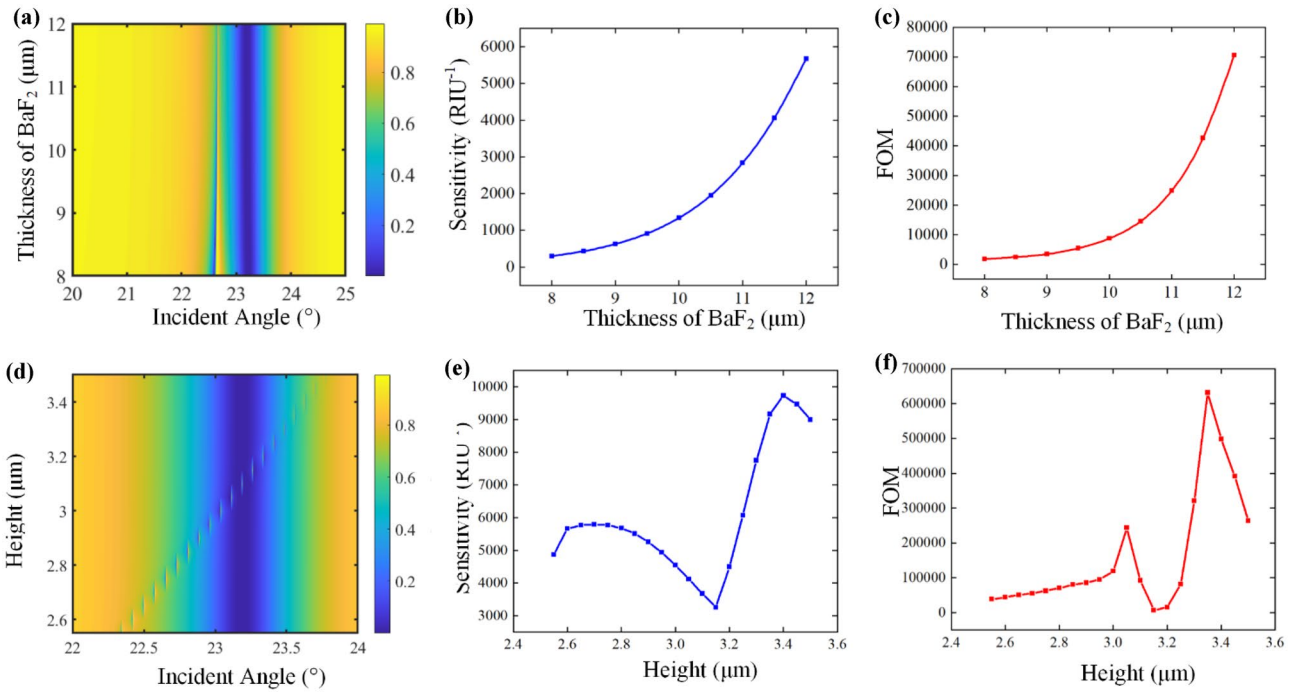

Fig. 5 Angle-resolved density plots of the reflectance with various **a** BaF_2 thickness and **d** height of ZnSe grating. **b**, **e** Sensitivity and **c**, **f** FOM as functions of BaF_2 thickness and height of ZnSe grating, respectively

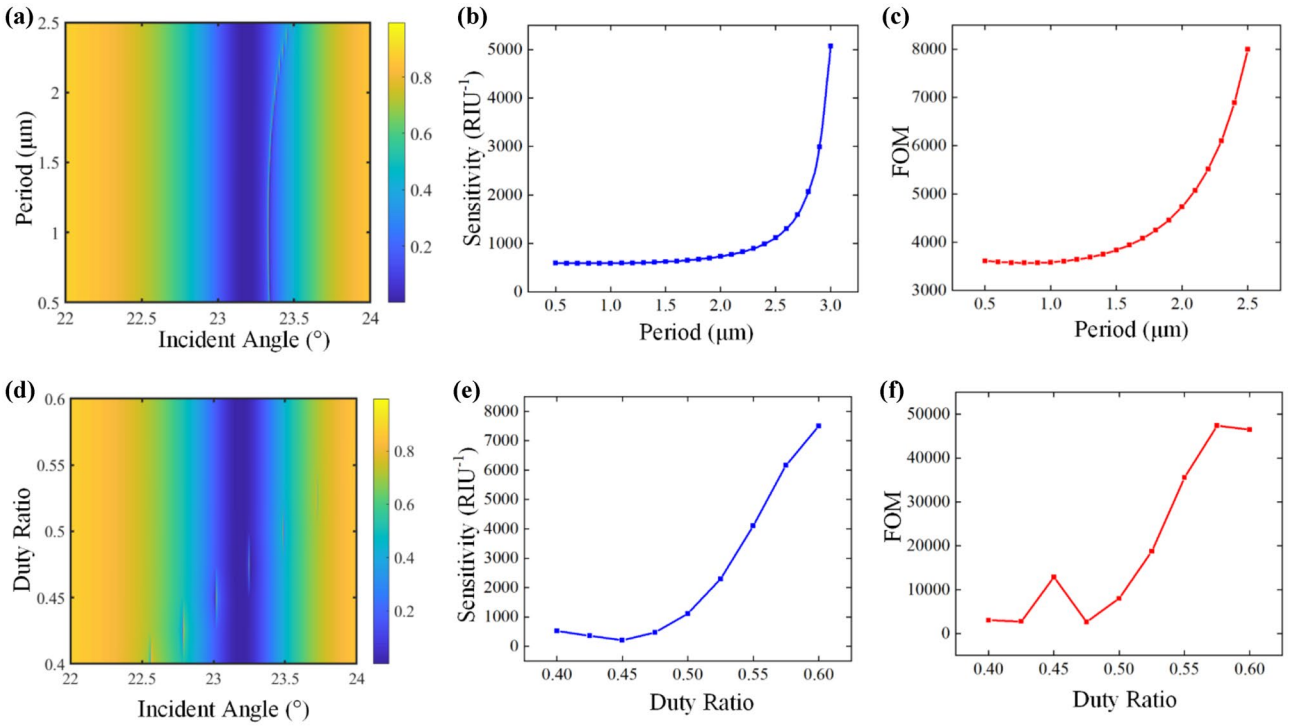

Fig. 6 Angle-resolved density plots of the reflectance with various **a** period and **d** duty ratio. **b**, **e** Sensitivity and **c**, **f** FOM as functions of period and duty ratio of ZnSe grating, respectively

its counterpart. With thicker BaF_2, the advantages of SWG-LRSPhR are more pronounced.

Discussion and Conclusion

Over the past years, researchers have made great efforts to develop the SPR-based sensors' unique advantages such as high sensitivity and miniaturization [36–41]. The devices reported in the above-mentioned references are mainly working in the visible or near-infrared (NIR) wavelength regime. Thus, the footprints are much smaller than the one in our manuscript, which operates in the mid-infrared (MIR) wavelength regime. To further reduce the size, materials supporting surface wave in the MIR, e.g., graphene and transition-metal dichalcogenide (TMDC), can be employed. In the future, optimizing the structure to produce more Fano resonances in single device [42] and introducing two-dimensional materials for enhancing the light-matter interaction are considered to improve the sensor performance [43].

In conclusion, a SWG-LRSPhR-coupled FR sensor has been proposed in MIR. RCWA method has been employed to optimize the structure parameters. Sensitivity and FOM have been employed to assess the sensing performance of RI. Numerical results have demonstrated clearly that the sensitivity and FOM of such a structure can reach 7496 RIU^{-1} and 46,432, respectively, which shows 6 times enhancement compared with the conventional WG-LRSPhR sensor. With such an excellent performance, the configuration can be a promising platform for biochemical sensing in the MIR.

Authors' Contributions

Tianye Huang and Xiangli Zhang directed the project; Dianhong Wang and Yuhan Wang designed the structure; Xiang Zhao analyzed field distribution; Yuhan Wang made the simulations; Yuhan Wang and Tianye Huang wrote the manuscript in consultation with Dianhong Wang, Xiangli Zhang, and Shuwen Zeng.

Funding

This work was supported by the Natural Science Foundation of Hubei Province under grant 2019CFB598; Wuhan Science and Technology Bureau under grant 2018010401011297; the Fundamental Research Funds for the Central Universities, China University of Geosciences (Wuhan) under grant 162301132703, G1323511794, and CUG2018JM16.

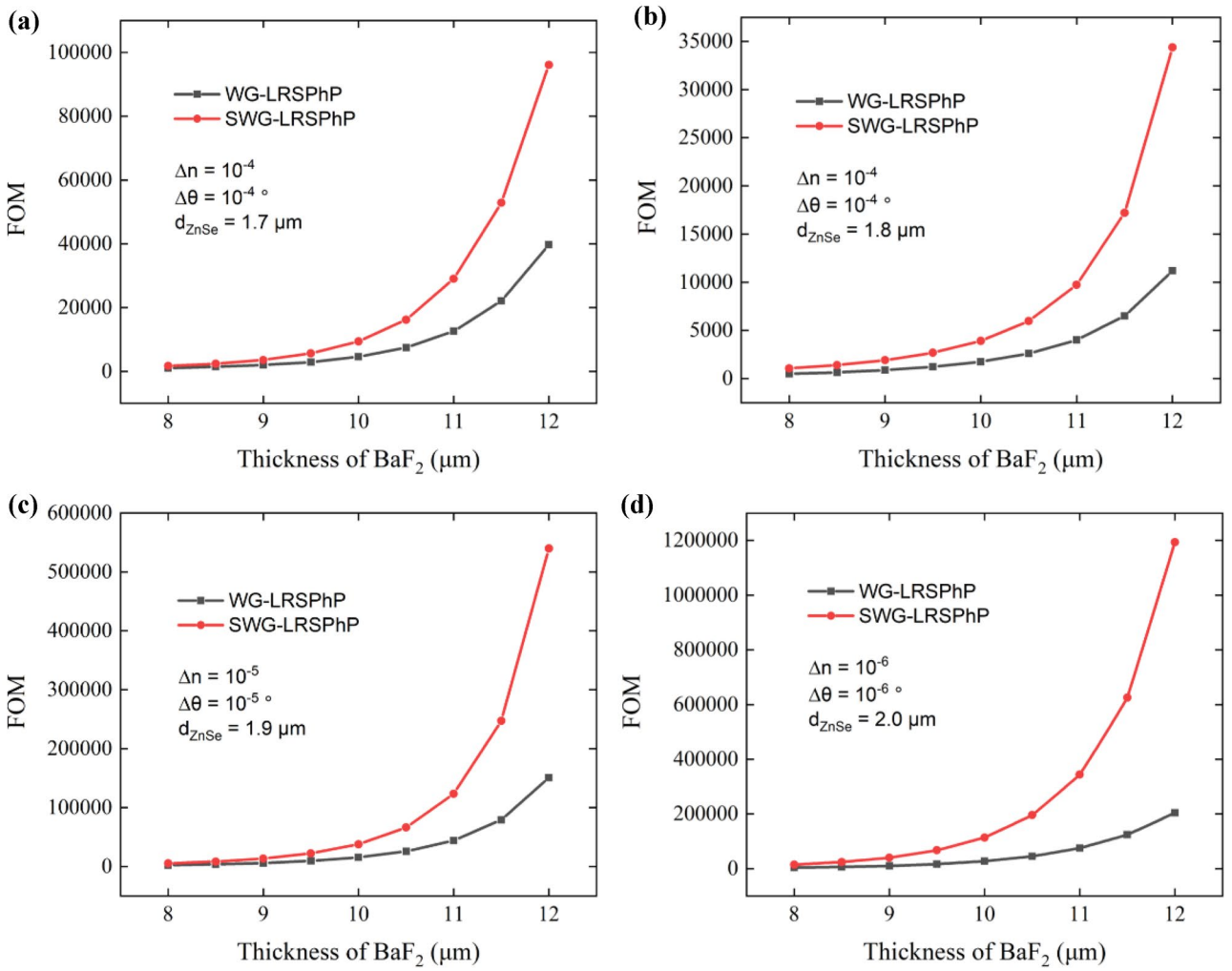

Fig. 7 Comparison of FOM between WG-LRSPhR and SWG-LRSPhR with different thicknesses of the BaF_2 layer

Data Availability The datasets used or analyzed during the current study are available from the corresponding author on reasonable request.

Compliance with Ethical Standard

Conflict of Interest The authors declare that they have no conflict of interest.

References

1. Mejía-Salazar JR, Oliveira ON (2018) Plasmonic Biosensing. Chem Rev 118:10617–10625
2. Liedberg B, Nylander C, Lunstrom I (1983) Surface plasmon resonance for gas detection and biosensing. Sensors and Actuators 4:299–304
3. Xu S, Zhan J, Man B, Jiang S, Yue W, Gao S, Guo C, Liu H, Li Z, Wang J (2017) Real-time reliable determination of binding kinetics of DNA hybridization using a multi-channel graphene biosensor. Nat Commun 8:14902
4. Chen ZQ, Chen Y, Xue ZH, Gao XD, Jia YA, Wang YJ, Lu YP, Zhang JY, Zhang M, Chen HX (2020) Insight into the inactivation mechanism of soybean Bowman-Birk trypsin inhibitor (BBTI) induced by epigallocatechin gallate and epigallocatechin: Fluorescence, thermodynamics and docking studies, Food Chem, 303
5. Masdor NA, Altintas Z, Shukor MY, Tothilll IE (2019) Subtractive inhibition assay for the detection of Campylobacter jejuni in chicken samples using surface plasmon resonance, Sci Rep-Uk, 9
6. Caldwell JD, Glembocki OJ, Francescato Y, Sharac N, Giannini V, Bezares FJ, Long JP, Owrutsky JC, Vurgaftman I, Tischler JG, Wheeler VD, Bassim ND, Shirey LM, Kasica R, Maier SA (2013) Low-loss, extreme subdiffraction photon confinement via silicon carbide localized surface phonon polariton resonators. Nano Lett 13:3690–3697
7. Zheng GG, Zhang HJ, Bu LB, Gao HY, Xu LH, Liu YZ (2018) Tunable Fano resonances in mid-infrared waveguide-coupled Otto configuration. Plasmonics 13:215–220

8. Khurgin JB, Sun G Scaling of losses with size and wavelength in nanoplasmonics and metamaterials, Appl Phys Lett, 99
9. Boltasseva A, Atwater HA (2011) Low-loss plasmonic metamaterials. Science 331:290–291
10. Dunkelberger AD, Ellis CT, Ratchford DC, Giles AJ, Kim M, Kim CS, Spann BT, Vurgaftman I, Tischler JG, Long JP, Glembocki OJ, Owrutsky JC, Caldwell JD (2018) Active tuning of surface phonon polariton resonances via carrier photoinjection. Nat Photonics 12:50
11. Caldwell JD, Lindsay L, Giannini V, Vurgaftman I, Reinecke TL, Maier SA, Glembocki OJ (2015) Low-loss, infrared and terahertz nanophotonics using surface phonon polaritons. Nanophotonics-Berlin 4:44–68
12. Zhu JQ, Ruan BX, You Q, Wu LM, Cai HZ, Dai XY, Xiang YJ (2018) Ultrasensitive Terahertz Imaging Sensors Based on the Strong Coupling of Surface Phonon Polariton and Graphene Surface Plasmon Polariton, Ieee Photonics J, 10
13. Ren XB, Ren K, Cai YX (2017) Tunable compact nanosensor based on Fano resonance in a plasmonic waveguide system. Appl Optics 56:H1–H9
14. Hayashi S, Nesterenko DV, Sekkat Z (2015) Fano resonance and plasmon-induced transparency in waveguide-coupled surface plasmon resonance sensors, Appl Phys Express, 8
15. Farmani H, Farmani A, Biglari Z, (2020) A label-free graphene-based nanosensor using surface plasmon resonance for biomaterials detection, Physica E, 116
16. Lu H, Liu XM, Mao D, Wang GX (2012) Plasmonic nanosensor based on Fano resonance in waveguide-coupled resonators. Opt Lett 37:3780–3782
17. Deng Y, Cao GT, Yang H, Li GH, Chen XS, Lu W (2017) Tunable and high-sensitivity sensing based on Fano resonance with coupled plasmonic cavities, Sci Rep-Uk, 7
18. Chen JJ, Gan FY, Wang YJ, Li GZ (2018) Plasmonic Sensing and Modulation Based on Fano Resonances, Adv Opt Mater, 6 (2018)
19. Xie Y, Chen Z, Wu Y, Zhao Y, Huang T, Cheng Z (2019) Bloch supermode interaction for high-performance polarization beam splitting. Opt Eng 58:095102
20. Xie Y, Chen Z, Yan J, Wu Y, Huang T, Cheng Z (2019) Combination of Surface Plasmon Polaritons and Subwavelength Grating for Polarization Beam Splitting, Plasmonics, 1–7
21. Huang TY, Xie Y, Wu YH, Cheng Z, Zeng SW, Ping PS (2019) Compact polarization beam splitter assisted by subwavelength grating in triple-waveguide directional coupler. Appl Optics 58:2264–2268
22. Halir R, Bock PJ, Cheben P, Ortega-Monux A, Alonso-Ramos C, Schmid JH, Lapointe J, Xu DX, Wanguemert-Perez JG, Molina-Fernandez I, Janz S (2015) Waveguide sub-wavelength structures: a review of principles and applications. Laser Photonics Rev 9:25–49
23. Luque-Gonzalez JM, Herrero-Bermello A, Ortega-Monux A, Molina-Fernandez I, Velasco AV, Cheben P, Schmid JH, Wang SR, Halir R (2018) Tilted subwavelength gratings: controlling anisotropy in metamaterial nanophotonic waveguides. Opt Lett 43:4691–4694
24. Bock PJ, Cheben P, Schmid JH, Lapointe J, Delâge A, Janz S, Aers GC, Xu D, Densmore A, Hall TJ (2010) Subwavelength grating periodic structures in silicon-on-insulator: a new type of microphotonic waveguide. Opt Express 18:20251–20262
25. Gervais A, Jean P, Shi W, Larochelle S (2019) Design of slow-light subwavelength grating waveguides for enhanced on-chip methane sensing by absorption spectroscopy. IEEE J Sel Top Quantum Electron 25:1–8
26. Xu G, Wang J, Ji Q, Yang M, Huang T, Pan J, Xie Y, Shum PP (2020) Design and analysis of slow-light Bloch slot waveguides for on-chip gas sensing. Journal of The Optical Society of America B-optical Physics 37:257–263
27. Neuner B, Korobkin D, Fietz C, Carole D, Ferro G, Shvets G (2009) Critically coupled surface phonon-polariton excitation in silicon carbide. Opt Lett 34:2667–2669
28. Zou XJ, Zheng GG, Chen YY, Xian FL, Xu LH (2018) Tunable and angle-independent thermal emitter based on surface phonon polariton mode in the mid-infrared range. Opt Mater 85:91–95
29. Zheng GG, Xu LH, Zou XJ, Liu YZ (2017) Excitation of surface phonon polariton modes in gold gratings with silicon carbide substrate and their potential sensing applications. Appl Surf Sci 396:711–716
30. Zheng G, Chen Y, Bu L, Xu L, Su W (2016) Waveguide-coupled surface phonon resonance sensors with super-resolution in the mid-infrared region. Opt Lett 41:1582–1585
31. Liu V, Fan S (2012) S4: A free electromagnetic solver for layered periodic structures. Comput Phys Commun 183:2233–2244
32. Hogan B, Lewis L, McAuliffe M, Hegarty SP (2019) Mid-infrared optical sensing using sub-wavelength gratings. Opt Express 27:3169–3179
33. Moharam MG, Gaylord TK (1981) Rigorous coupled-wave analysis of planar-grating diffraction. Journal of the Optical Society of America 71:811–818
34. Moharam MG, Grann EB, Pommet DA, Gaylord TK (1995) Formulation for stable and efficient implementation of the rigorous coupled-wave analysis of binary gratings. Journal of The Optical Society of America A-optics Image Science and Vision 12:1068–1076
35. Chen J, Li Z, Zou Y, Deng Z, Xiao J, Gong Q (2013) Coupled-resonator-induced Fano resonances for plasmonic sensing with ultra-high figure of merits. Plasmonics 8:1627–1631
36. Moncada-Villa E, Oliveira ON, Mejía-Salazar JR (2019) ε-Near-zero materials for highly miniaturizable magnetoplasmonic sensing devices. The Journal of Physical Chemistry C 123:3790–3794
37. Girón-Sedas JA, Reyes Gómez F, Albella P, Mejía-Salazar JR, (2017) Oliveira ON Giant enhancement of the transverse magneto-optical Kerr effect through the coupling of ε-near-zero and surface plasmon polariton modes, Physical Review B, 96 075415
38. Caballero B, Garciamartin A, Cuevas J (2016) Hybrid magnetoplasmonic crystals boost the performance of nanohole arrays as plasmonic sensors. ACS Photonics 3:203–208
39. Chien F, Lo J, Zhang X, Cubukcu E, Luo Y, Huang K, Tang X, Chen C, Chen C, Lai K (2018) Nitride-based microarray biochips: a new route of plasmonic imaging. ACS Appl Mater Interfaces 10:39898–39903
40. Diaz-Valencia BF, Mejía-Salazar JR, Oliveira ON, Porras-Montenegro N, Albella P (2017) Enhanced transverse magneto-optical Kerr effect in magnetoplasmonic crystals for the design of highly sensitive plasmonic (bio)sensing platforms. ACS Omega 2:7682–7685
41. Ignatyeva DO, Knyazev GA, Kapralov PO, Dietler G, Sekatskii SK, Belotelov VI (2016) Magneto-optical plasmonic heterostructure with ultranarrow resonance for sensing applications. Sci Rep-Uk 6:28077–28077
42. Zhao Z, Cheng Z, Zhu M, Huang T, Zeng S, Pan J, Song C, Wang Y, and Shum PP (2020) "Study on the dual-Fano resonance generation and its potential for self-calibriated sensing", Optics Express, to be appeared
43. Zhao X, Huang T, Ping P, Wu X, Huang P, Pan J, Wu Y, Cheng Z (2018) Sensitivity enhancement in surface plasmon resonance biochemical sensor based on transition metal dichalcogenides/graphene heterostructure. Sensors 18:2056

Publisher's Note Springer Nature remains neutral with regard to jurisdictional claims in published maps and institutional affiliations.